Journal of Materials Chemistry C

ROYAL SOCIETY OF CHEMISTRY

PAPER

View Article Online
View Journal | View Issue

Cite this: J. Mater. Chem. C, 2021, 9, 15212

Strong Fermi-level pinning at metal contacts to halide perovskites†

Kootak Hong,[ab] Ki Chang Kwon,‡[a] Kyoung Soon Choi,[c] Quyet Van Le,[d] Seung Ju Kim,[a] Ji Su Han,[a] Jun Min Suh,[a] Soo Young Kim,*[e] Carolin M. Sutter-Fella*[b] and Ho Won Jang*[af]

Received 19th July 2021,
Accepted 12th October 2021

DOI: 10.1039/d1tc03370k

rsc.li/materials-c

The performance of halide perovskite-based electronic and optoelectronic devices is often related to interfacial charge transport. To shed light on the underlying physical and chemical properties of $CH_3NH_3PbI_3$ ($MAPbI_3$) in direct contact with common electrodes Al, Ti, Cr, Ag, and Au, the evolution of interfacial properties and Fermi level pinning is systematically studied. Given a unique experimental facility, pristine interfaces without any exposure to ambient air were prepared. We observe aggregation of substantial amounts of metallic lead (Pb^0) at the metal/$MAPbI_3$ interface, resulting from the interfacial reaction between the deposited metal and iodine ions from $MAPbI_3$. It is found that the Schottky barrier height at the metal/$MAPbI_3$ interface is independent of the metal work function due to strong Fermi level pinning, possibly due to the metallic Pb^0 aggregates, which act as interfacial trap sites. The charge neutrality level of $MAPbI_3$ is consistent with the energy level of Pb^0-related defects, indicating that Pb^0 interfacial trap states can be nonradiative recombination sites. This work underlines that control of chemical bonding at interfaces is a key factor for designing future halide perovskite-based devices.

Introduction

After the first report on organolead halide perovskites (with $CH_3NH_3PbI_3$ being the forerunner compound) as light absorber materials in 2009,[1] there have been numerous efforts to improve performance and stability of halide perovskite-based solar cells.[2–6] Unprecedented rapid developments led to power conversion efficiencies (PCE) exceeding 25% within about a decade of research.[7] Therefore, halide perovskites are considered to be promising candidates for solving the impending energy shortage owing to their exceptional optical and charge transport properties.[8–12] Moreover, their properties including bandgap, doping concentration, electronic conductivity and ionic conductivity, can be easily tuned through alloying using facile solution synthesis methods.[13–15] In this regard, halide perovskites have attracted considerable interest due to their potential applications in optoelectronic and electronic devices,[16] such as light-emitting diodes,[17] lasers,[18] photodetectors,[19] field-effect transistors (FETs),[20] resistive-switching random access memories (ReRAMs)[21] and artificial synapses.[22]

Interfaces are of utmost importance not only for device functioning but also for device performance and stability.[23,24] As an example, the energy level alignment at heterointerfaces such as charge transport layer (CTL)/perovskite or metal/perovskite is critical for efficient charge carrier separation and transport. Most studies thus far have focused on CTL/perovskite interfaces,[25–27] while less attention has been given to metal/perovskite interfaces.[28–31] The latter, however, is of importance for electronic and optoelectronic devices such as FETs, memories and photodetectors, determining contact resistance, charge transfer behavior and on/off ratio,[32–34] as well as in solar cells operating without electron or hole selective contacts in order to reduce device complexity and fabrication cost.[35,36] Previous studies have mainly investigated the metal/perovskite interfaces with the motivation of understanding the long-term stability of the halide perovskite-based device where diffusion of metals through CTLs and subsequent reaction with

[a] Department of Materials Science and Engineering, Research Institute of Advanced Materials, Seoul National University, Seoul 08826, Republic of Korea. E-mail: hwjang@snu.ac.kr
[b] Joint Center for Artificial Photosynthesis, Chemical Sciences Division, Lawrence Berkeley National Laboratory, Berkeley, California 94720, USA. E-mail: csutterfella@lbl.gov
[c] National Research Facilities and Equipment Center, Korea Basic Science Institute, Daejeon 34133, Republic of Korea
[d] Institute of Research and Development, Duy Tan University, Da Nang 550000, Vietnam
[e] Department of Materials Science and Engineering, Korea University, Seoul 02841, Republic of Korea. E-mail: sooyoungkim@korea.ac.kr
[f] Advanced Institute of Convergence Technology, Seoul National University, Suwon, 16229, Republic of Korea

† Electronic supplementary information (ESI) available. See DOI: 10.1039/d1tc03370k

‡ Present address: Center for convergence property measurement, Korea Research Institute of Standards & Science (KRISS), Daejeon 34113, Republic of Korea.

halide perovskites lead to performance degradation.[28,29] To this end, there are however, contradicting reports on the contact type of metal/halide perovskite interfaces.[36–39] For example, Peng *et al.* and Gu *et al.* observed Ohmic conduction behavior in devices with an Au/$CH_3NH_3PbI_3$ ($MAPbI_3$) interface,[36,37] while Liu *et al.* and Lin *et al.* reported the formation of Schottky contacts at the same material interface.[38,39] The discrepancy between various studies might be attributed to different halide perovskite preparation methods leading to different stoichiometries and surface chemistry, measurement conditions, mixed ionic-electronic conduction behavior found in halide perovskites, and uncontrolled exposure to moisture and light irradiation that can impact the metal/halide perovskite interface.[19,23,40] Therefore, reliable characterizations of metal/halide perovskite interfaces under well-controlled condition is challenging but needed to understand the pristine interface formation, existence of surface trap states, and energy level alignment which dominate device performance. To do so, highly surface sensitive X-ray photoemission spectroscopy (XPS) has proven to be an appropriate characterization technique for the evaluation of physical and chemical interface properties of halide perovskites without the need for an externally applied bias voltage.[23,41,42]

In this work, we present an experimental study on the interfacial structure evolution and origin of strong Fermi level pinning at pristine metal/$MAPbI_3$ interfaces by means of photoelectron spectroscopy. Formation of a pristine interface was enabled by using a glovebox equipped with a thermal evaporator and a direct transfer system to an XPS measurement chamber without exposing the samples to ambient air at any point. The common metal electrodes Al. Ti, Cr, Ag, and Au were selected to investigate the relationship of metal/$MAPbI_3$ interfaces as low and high work function metals from 4.1 to 5.2 eV. We found that a substantial amount of metallic lead (Pb^0) is formed at the interfaces irrespective of metal electrode material. In addition, by chemical profiling we detect metal–iodine compounds at the interface indicating that the formation of Pb^0 aggregates can be attributed to the chemical reaction between iodine in $MAPbI_3$ and the interfacing metal layer. The Pb^0 aggregates induce Fermi-level pinning at the metal/$MAPbI_3$ interfaces, suggesting that the Fermi-level pinning at $MAPbI_3$ is mainly determined by the interfacial trap states rather than metal-induced gap states. The charge neutrality level of $MAPbI_3$ is consistent with the energy level of Pb^0-related defects, which are nonradiative recombination sites. These results clearly show that the Pb^0 aggregates play a key role in deteriorating charge transfer efficiency and determining the electrical properties of metal/$MAPbI_3$ interfaces. This study provides new insights for designing high performance halide perovskite-based electronic and optoelectronic devices.

Results and discussion

To investigate the physical and chemical status of metal/halide perovskite interfaces without contamination and degradation, we fabricated and characterized metal/halide perovskite thin films under a nitrogen atmosphere and ultrahigh vacuum, as illustrated in Scheme 1. The most studied halide perovskite composition, $MAPbI_3$, and typical metal electrodes (Al, Ti, Cr, Ag, and Au) with work functions from 4.1 eV to 5.2 eV are selected (Fig. 1a).[43] First, $MAPbI_3$ thin films were synthesized on Si substrates using one-step spin coating of a precursor solution in an N_2-filled glove box (H_2O <0.1 ppm, O_2 <0.1 ppm). The samples were prepared without antisolvent dripping or additional treatments to rule out the possibility of modification on surface chemistry of $MAPbI_3$ due to antisolvent and interface engineering.[44] The spin-coated solution was crystallized by annealing at 110 °C for 10 min. The $MAPbI_3$ thin films show tetragonal crystal structure and similar morphology with previous reports (Fig. S1, ESI†).[45] To form pristine metal/$MAPbI_3$ interfaces, 5–80 Å thick (mass thickness) metal films (Al, Ti, Cr, Ag, and Au) were thermally evaporated onto the $MAPbI_3$ surface in a glovebox-integrated metal evaporation chamber. The integrated evaporation chamber allows for the direct formation of pristine interfaces. The metal/$MAPbI_3$ stacks were immediately transferred from the glovebox to an ultrahigh vacuum spectroscopy system (10^{-11} mbar) using an in-line transfer, thus avoiding air, moisture, and light exposure. Next, the physical and chemical properties of the metal/$MAPbI_3$ interfaces were investigated by UPS and XPS.

Fig. 1b–f show the evolution of the UPS spectra at the secondary cutoff region and valence band region with the gradual deposition of various metal thin films. All the spectra were normalized to the same height. The secondary cut off energy was determined by linear extrapolation of the leading edge of the spectra.[46] The shifts of secondary cut off energy are highlighted with shaded areas and arrows in the spectra. The vacuum level (VL) is obtained from the difference between the secondary cutoff energy and the photon energy (21.22 eV). For bare $MAPbI_3$ thin films, it is found that the work function (WF) is 4.35 eV and the energy difference between the Fermi level and the valence band maximum ($E_F - E_V$) is 1.43 eV, comparable to those previously reported in literature.[41,47] With a bandgap of 1.53 eV (Fig. S2, ESI†), the surface of $MAPbI_3$ thin films studied in this work exhibits pronounced n-type character in agreement with previous reports.[41,42,47] With the subsequent

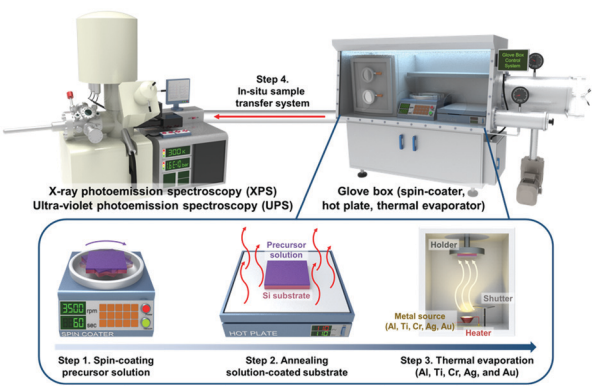

Scheme 1 Schematic illustration for preparation and characterization process of metal/$MAPbI_3$ thin films.

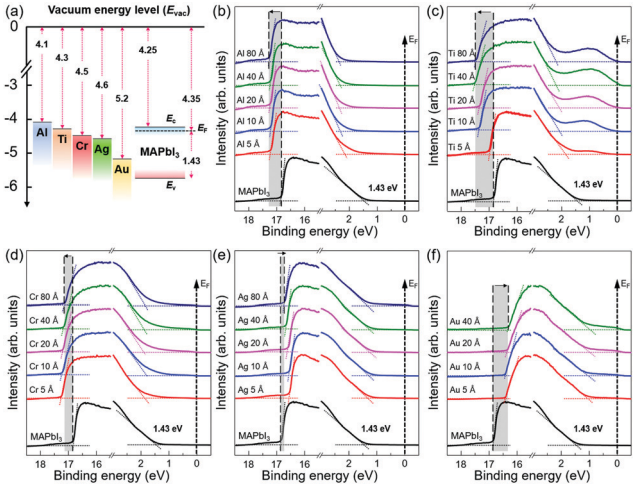

Fig. 1 (a) Energy level scheme for isolated metals and $MAPbI_3$ prior to interface formation used in this study. The work function is given for each material and the bandgap of $MAPbI_3$ is included with 1.53 eV. E_c, E_v, and E_F refer to the conduction, valence band, and the Fermi level, respectively. Thickness dependent UPS spectra of metal/$MAPbI_3$ thin films showing the cutoff region and the VBM region. (b) Al/$MAPbI_3$ thin films, (c) Ti/$MAPbI_3$ thin films, (d) Cr/$MAPbI_3$ thin films, (e) Ag/$MAPbI_3$ thin films, and (f) Au/$MAPbI_3$ thin films. The shaded areas and arrows in the spectra are guides to the eye and represent the shift of secondary cut off energy of $MAPbI_3$ upon the metal deposition.

metal deposition of 5 Å, the VL of the metal/$MAPbI_3$ thin films show an abrupt change. For Al, Ti, and Cr, the VL decreases to 3.99 eV, 4.23 eV, and 3.94 eV, whereas, for Ag and Au, the VL increases to 4.66 eV and 4.78 eV, respectively. As the thicknesses of the metal layers increase to 80 Å, the VL of metal/$MAPbI_3$ saturate at 3.94 eV, 3.71 eV, 4.02 eV, 4.48 eV, and 4.90 eV for Al, Cr, Ti, Ag, and Au, respectively. The VL shift at the metal/$MAPbI_3$ interfaces reveals that charge transfer occurs between the deposited metals and $MAPbI_3$ thin films.[48] Al, Ti, and Cr deposition on $MAPbI_3$ leads downward VL shift, indicating that electrons are transferred from Al, Ti, and Cr to $MAPbI_3$. On the other hand, the upward VL shift with Ag and Au deposition means electron transfer occurs from $MAPbI_3$ thin films to the metal (Ag and Au). The valence band maximum (VBM) is determined by a linear extrapolation of valence band onset subtracted to the background around Fermi level.[46] The valence band spectra show the similar trend with the evolution of secondary electron cut off with the increasing metal deposition (Fig. 1b–f and Fig S3 in ESI†). In addition, it can be seen that the metallic Fermi edge becomes pronounced and the perovskite-related features gradually attenuated with increasing metal thickness (Fig. S4, ESI†).

In order to further understand the energy level evolution and the interface reaction at the metal/$MAPbI_3$ interfaces, we performed XPS analysis to investigate the chemical characteristics and the shift in the core-level spectra of $MAPbI_3$ after the metal deposition (Fig. S5 and S6, ESI†). It can be known that the bare $MAPbI_3$ and metal/$MAPbI_3$ stacks remained free of contaminations during the whole experiment (Fig. S5, ESI†). Fig. 2 displays the evolution of the Pb $4f_{7/2}$ core level spectra as a function of the deposited metal thickness. The Pb 4f spectrum is attenuated at 80 Å Ti due to the limited probing depth of XPS. All the spectra were normalized to the same height to see changes in peak shapes and position clearly and the peak positions were obtained by Gaussian–Lorentzian fitting. For bare $MAPbI_3$, the Pb $4f_{7/2}$ core level presents two peaks located at 138.24 eV and 136.74 eV (Fig. S7, ESI†). The larger Pb $4f_{7/2}$ peak is attributed to the Pb–I bonds in $MAPbI_3$, while the smaller Pb $4f_{7/2}$ peak is a representative feature of metallic lead (Pb^0).[49,50] The formation of metallic Pb^0 in the bare $MAPbI_3$ is associated with losses of iodine atoms during sample annealing.[47] After metal deposition, the Pb $4f_{7/2}$ core level clearly shifts toward lower binding energies. It is attributed to the formation of Pb^0 at the metal/$MAPbI_3$ interfaces, indicating redox reactions occur at the interface. The total shift of Pb $4f_{7/2}$ to lower binding energy is measured to be 0.2 ± 0.1 eV, indicating the upward band bending in $MAPbI_3$ thin films induced by the metal deposition. Notably, it is evident that the metallic Pb^0 peak (136.74 eV) becomes pronounced with increasing metal thickness. To evaluate the relative amount of Pb^0, the evolution of the ratio of Pb^{2+} to Pb^0 (Pb^{2+}/Pb^0) as a function of deposited metal thickness is plotted in Fig. 2f. For bare $MAPbI_3$, the Pb^{2+}/Pb^0 is 27.77. The Pb^{2+}/Pb^0 is drastically decreased after 5 Å layer of metal deposition and saturates at 0.59 (Al), 0.98 (Ti), 1.07 (Cr), 4.21 (Ag), and 2.51 (Au) with increasing the deposited metal thickness, respectively. This trend indicates that Pb^0 becomes enriched at the metal/$MAPbI_3$ interface possibly due to charge transfer between the deposited metal layers and $MAPbI_3$ thin films.

To provide further information on the interaction between the deposited metal layers and the $MAPbI_3$ thin films, we also obtained the Al 2p, Ti 2p, Cr 2p, Ag 3d and Au 4f core level spectra (Fig. 3). From the evolution of the metal core level spectra, it can be derived that the deposited metals were (partially) oxidized. It indicates that a redox reaction occurs at the metal/$MAPbI_3$ interfaces resulting from the charge transfer between the deposited metal and $MAPbI_3$ thin films. For example, we can find the dominant Al^{3+} (74.7 eV) and Ag^+ (367.8 eV) peaks in Al 2p and Ag $3d_{5/2}$ spectra, which are associated to the Al and Ag component in aluminium halides and silver halides, respectively (Fig. 3a and d).[51] The Au $4f_{7/2}$ spectra can be deconvoluted into two distinct components centered at 83.8 eV and 85.1 eV, which are ascribed to Au^0 and Au +, respectively (Fig. 3e).[52] The oxidized Al, Ag, or Au layers on $MAPbI_3$ and the formation of Pb^0 through reduction of Pb^{2+} suggest a redox reaction at Al/$MAPbI_3$, Ag/$MAPbI_3$, Au/$MAPbI_3$ interfaces. In addition, it was observed that the peaks with higher binding energies, compare Al 2p, Ti 2p, and Cr 2p spectra in Fig. 3a–c, corresponding to higher oxidation states of the metals, are more dominant at low metal thickness (5 Å) as compared to 80 Å. With increasing metal layer thickness, the fraction of metallic component (Al^0, Ti^0, and Cr^0) becomes stronger due to increasing contribution of neutral metals. The changes in the dominant oxidation states can be seen more clearly in metals with multivalent oxidation states, here for Ti and Cr.

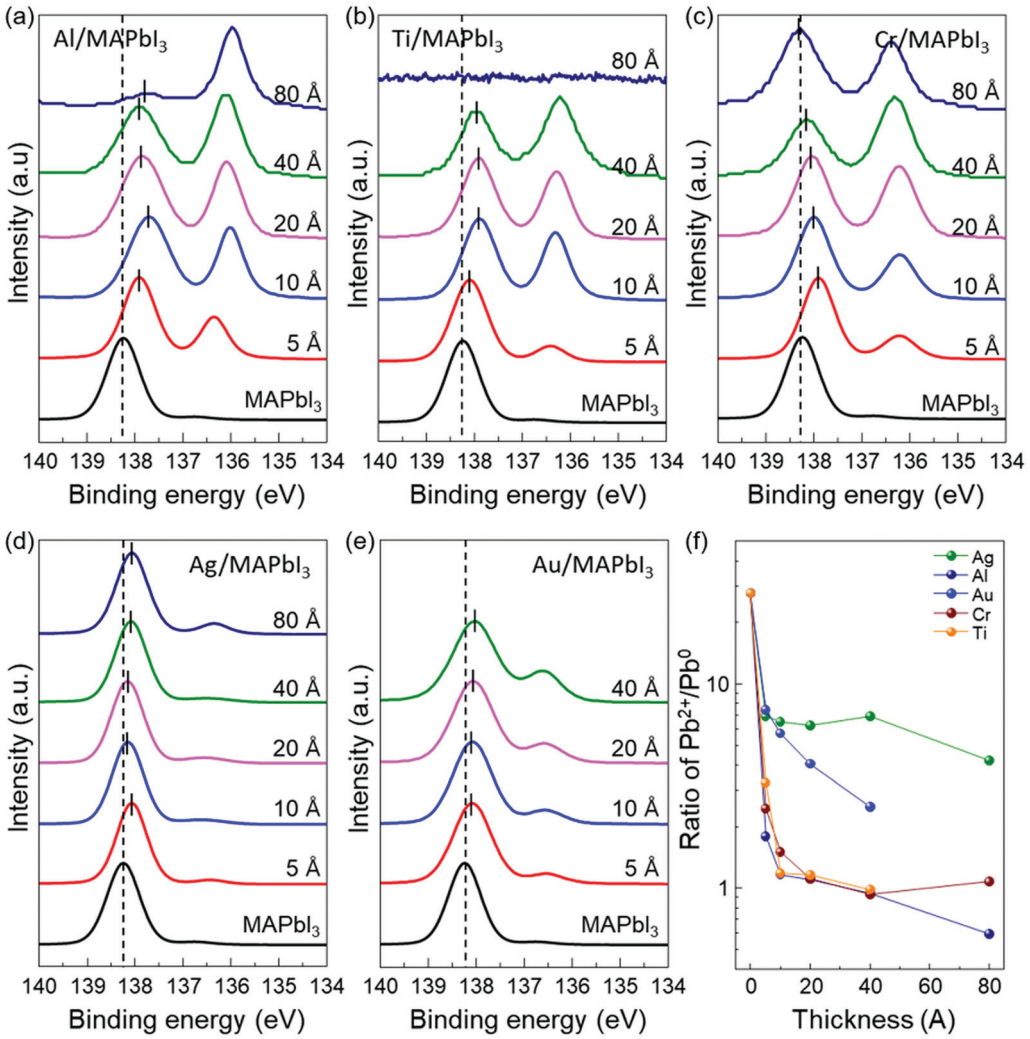

Fig. 2 The evolution of Pb $4f_{7/2}$ XPS peaks of the metal/$MAPbI_3$ thin films as a function of the deposited metal thickness. (a) Al/$MAPbI_3$ thin films, (b) Ti/$MAPbI_3$ thin films, (c) Cr/$MAPbI_3$ thin films, (d) Ag/$MAPbI_3$ thin films, and (e) Au/$MAPbI_3$ thin films. The dashed lines mark the core levels Pb $4f_{7/2}$ of the pristine $MAPbI_3$ thin films. (f) The ratio of Pb^{2+}/Pb^0 with increasing thickness of the deposited metal.

The direct comparison of XPS spectra and their change with increasing metal layer thickness underline the redox reaction at the metal/$MAPbI_3$ interface leading to the formation of metallic Pb. Previously, Liu *et al.* reported that no metallic Pb^0 was observed at Au/$MAPbI_3$ interfaces and this was explained by partial charge transfer in absence for evidence that would indicate a redox reaction.[38] These differences are due to factors affecting the surface chemistry of halide perovskites, such as different synthesis methods, uncontrolled measurement conditions and degradation by air exposure or light illumination. Our findings indicate that the charge transfer leading to formation of Pb^0 at the metal/$MAPbI_3$ interfaces can be attributed to interface reactions between the deposited metal and halide perovskite, while the probability for $MAPbI_3$ degradation driven by air, moisture, or light is relatively low given our experimental setup and not exposing the sample to air at any point.

To further investigate the underlying interfacial chemistries of the metal/$MAPbI_3$ interfaces, time-of-flight secondary ion mass spectroscopy (ToF-SIMS) is employed to study the elemental distribution in the metal/$MAPbI_3$ stacks. Fig. 4 shows the ToF-SIMS depth profiles of relative element distributions in Ag/$MAPbI_3$, Au/$MAPbI_3$, and Ti/$MAPbI_3$ stacks. The boundaries of each layer were identified by the intensity of detected ions, as reported in previous studies.[53,54] Al^-, Au^-, and Ti^- ions are selected to identify the deposited metal layers, Pb^- for Pb^0 aggregates, PbI_3^- for the $MAPbI_3$ thin films, Si^- for the substrates. The maximum signals of AgI^-, AuI^-, and TiI^- are observed at the Ag/$MAPbI_3$, Au/$MAPbI_3$, and Ti/$MAPbI_3$ interfaces, indicating a chemical reaction between the deposited metals and iodine from the $MAPbI_3$ surface. The formation of metal–iodine compounds is attributed to thermodynamically stronger bonds as compared to metal–metal bonds.[43] In addition, the ToF-SIMS result of the bare $MAPbI_3$ film (Fig. S8, ESI†) reveals that the concentration of Pb^0 is higher in the bulk than at the surface, which is in good agreement with the Pb^0 distribution in bare $MAPbI_{3-x}Cl_x$ films reported by

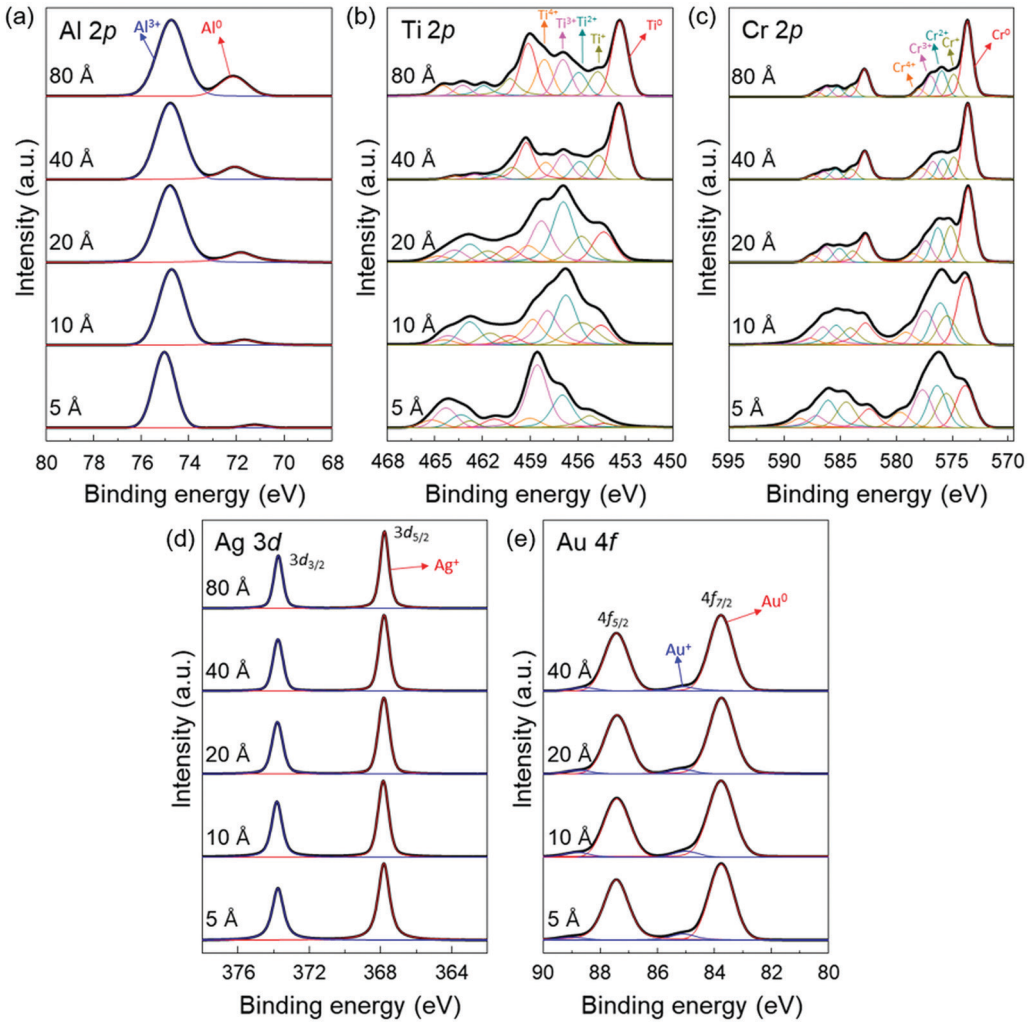

Fig. 3 Thickness dependent XPS spectra of (a) the Al 2p peaks in the Al/$MAPbI_3$ thin films, (b) the Ti 2p peaks in the Ti/$MAPbI_3$ thin films, (c) the Cr 2p peaks in the Cr/$MAPbI_3$ thin films, (d) the Ag 3d peaks in the Ag/$MAPbI_3$ thin films, and (e) the Au 4f peaks in the Au/$MAPbI_3$ thin films.

Sadoughi *et al.*[50] However, the concentration of Pb^0 at metal/$MAPbI_3$ interfaces is comparable with that at bulk $MAPbI_3$. It indicates that a substantial amount of Pb^0 is existed at metal/$MAPbI_3$ interfaces, consistent with XPS results.

Overall, our XPS and ToF-SIMS results provide evidence that the redox reaction between $MAPbI_3$ and all investigated metals occurs. It has been reported that thermodynamically unfavorable reactions can occur at metal/semiconductor, especially metal/Pb(Zr,Ti)O_3 interface, due to the heat of condensation of metal atoms.[55–57] However, the formation of metal–iodine bond is thermodynamically favor due to the negative formation enthalpy and energy barrier,[43] resulting in the formation of Pb^0 state at metal/$MAPbI_3$ interfaces (Table S1, ESI†). Generally, it is believed that Ag has higher reactivity with halide perovskite compared to other metals.[28,58,59] The energy barrier for Ag and standard enthalpy of formation of AgI are less negative than those of Al, Cr and Ti. This trend is in good agreement with our experimental results. The difference between our results and the previous reports is attributed to the sample preparation and measurement methods. Our samples were investigated immediately after metal deposition without exposure to air and moisture, whereas the previous reports focused on the degradation mechanism of Ag/halide perovskite interfaces under air/humid conditions for more than several days. We speculate that the following reactions occur at the interface between $MAPbI_3$ and the metal, M (with valency, z) account for the charge transfer of electrons due to the formation of the metal–iodine compounds which reduce Pb^{2+} in $MAPbI_3$ to Pb^0.

$$M_0 + zI^- \rightarrow MI_z + ze^- \quad (1)$$

$$Pb^{2+} + 2ze^- \rightarrow Pb^0 \quad (2)$$

It has been reported that Pb^0 in pristine halide perovskites acts as a donor-like surface state, which pins E_F at the surface.[41,42] Thus we speculate that the Pb^0 formed at the metal/$MAPbI_3$ interface could influence the charge transport behavior. Next, we extract the effective Schottky barrier height (SBH) for electrons, which is one of the important parameters determining charge transfer efficiency, from the Pb $4f_{7/2}$ core

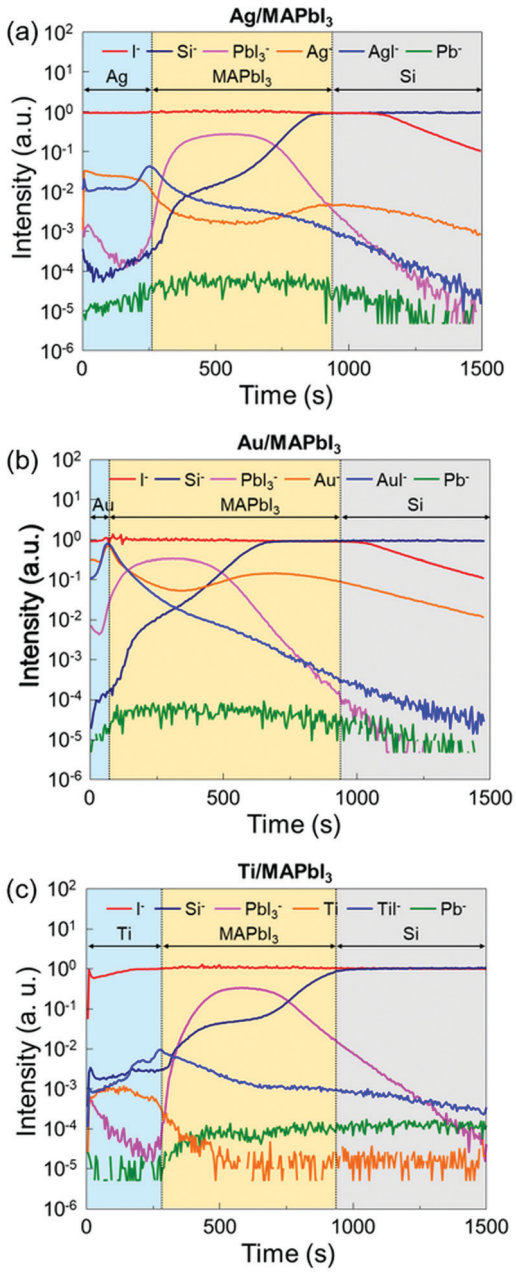

Fig. 4 ToF-SIMS depth profiles of (a) the Ag/$MAPbI_3$, (b) the Au/$MAPbI_3$, and (c) the Ti/$MAPbI_3$ stacks.

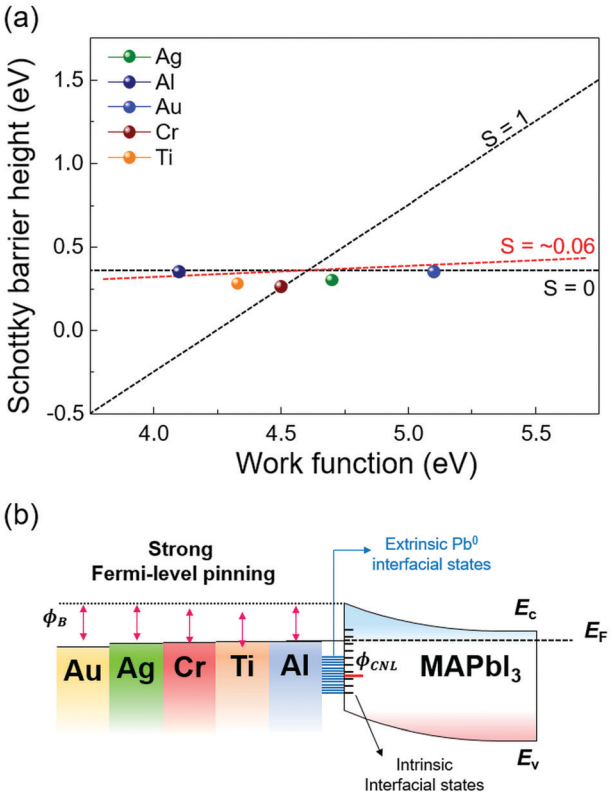

Fig. 5 (a) Extracted Schottky barrier heights of $MAPbI_3$ for the various metal work functions, showing the pinning factor $S \sim 0.06$ when the deposited metal thickness is 40 Å (red dashed line). (b) Band diagram of metal/$MAPbI_3$ interfaces with five different metals.

level shifts in the metal/$MAPbI_3$ interfaces using the following equation:[60]

$$\phi_B = E_g - E_v^i + (E_{core}^i - E_{core}^{metal}) = E_g - (E_{core}^{metal} - E_{VC}) \quad (3)$$

where ϕ_B is the SBH, E_g is the bandgap of $MAPbI_3$ (1.53 eV), E_{core}^{metal} is the binding energy of the core level peak after metal deposition, E_{core}^i is the initial binding energy of the core level peak (138.24 eV), E_v^i is the initial binding energy of the VBM of $MAPbI_3$, and E_{VC} is equal to $(E_{core}^i - E_v^i)$.

The extracted SBH values of the metal/$MAPbI_3$ thin films are plotted as a function of the metal work function, as shown in Fig. 5a. The WF and SBH variations depending on the thickness of each metal appear as error bars in the *x*-axis and in the *y*-axis. It is apparent that the extracted SBHs are independent of metal work functions. To estimate the pinning factor (S) and charge neutrality level (ϕ_{CNL}), we perform a linear fit using the Schottky–Mott law and the Sze model.[61] The details in the fitting method are described in ESI.† The value of S varies from 1 for ideal interface without Fermi-level pinning to 0 for a strongly pinned interface. The obtained S value for the metal/$MAPbI_3$ interfaces is 0.06 when the thickness of the deposited metal layer is 40 Å and the ϕ_{CNL} is estimated to be 4.63 eV from the vacuum level, close to the Fermi level and above valence band maximum. This result reveals a strong Fermi-level pinning at the metal/$MAPbI_3$ interface, therefore an ohmic contact cannot be formed between $MAPbI_3$ and the metals investigated here (Fig. 5b).

We also calculated the density of the gap states (D_g) at the metal/$MAPbI_3$ interfaces using the Sze model because the gap states is known to induce Fermi-level pinning at metal/semiconductor junctions (details are given in ESI†).[61,62] The calculated gap D_g are the sum of the density metal-induced gap states (D_{MIGS}) and interface trap states (D_{IT}), the D_g, D_{MIGS}, and D_{IT} are estimated to be 2.09×10^{15}, 4.16×10^{13}, and 2.05×10^{15} eV^{-1} cm^{-2}, respectively. This result indicates that the interface trap states mainly cause the strong Fermi-level

pinning at metal/$MAPbI_3$ interfaces. Strikingly, the density of calculated gap states at the metal/$MAPbI_3$ interfaces is two orders of magnitude larger than the previously reported surface state density of bare $MAPbI_3$ ($\sim 10^{13}$ eV^{-1} cm^{-2}).[63] Probably, the formation of Pb^0 due to the redox reaction between the deposited metal and iodine in $MAPbI_3$ contributes to the difference in D_g. This result indicates that the metal/$MAPbI_3$ interfaces suffer from low charge transfer efficiency due to the Pb^0-interface trap state-induced strong Fermi-level pinning. Therefore, to enable efficient charge transport at the meal/$MAPbI_3$ interfaces, the redox reaction resulting in the formation of extrinsic interface trap state should be suppressed.

Furthermore, our experimental ϕ_{CNL} of $MAPbI_3$ is in agreement with the theoretical value of the Pb^0-related defect energy levels of $MAPbI_3$.[64] It means that the Pb^0 trap states at the metal/$MAPbI_3$ interfaces can act as nonradiative recombination sites, resulting in performance degradation of halide perovskite-based devices.[50] It has been reported that different surface termination leads to changes in Fermi-level pinning at the surface of pristine halide perovskite due to the different amount of surface states.[63] However, it is uncertain that controlled surface termination of halide perovskite surface can suppress the reaction at the interface between the metal and halide perovskite. To reduce the Pb^0-interface trap states at the metal/$MAPbI_3$ thin films, an interlayer such as graphene and polymer thin films, which can prevent the reaction between the metal and halide perovskite, should be inserted at the interface.[53,65]

Conclusions

In summary, we have experimentally investigated the evolution of interfacial properties and Fermi-level pinning at the interface between $MAPbI_3$ and Al, Ti, Cr, Ag, and Au. XPS measurements indicate accumulation of Pb^0 at the metal/$MAPbI_3$ interfaces with subsequently increasing metal layer thickness. The formation of Pb^0 aggregates at the interfaces is attributed to the interfacial reaction between the deposited metal and iodine ion from $MAPbI_3$, confirmed by ToF-SIMS analysis. Based on the core level shift in metal/$MAPbI_3$ interfaces, we obtained the effective Schottky barrier heights and the pinning factor between the metals and $MAPbI_3$. The pinning factor of $MAPbI_3$ is 0.06, indicating that Schottky barrier heights at the metal/$MAPbI_3$ interfaces are independent with metal work function. The charge neutrality level of $MAPbI_3$ is 4.62 eV less than 0.3 eV from the E_F, consistent with Pb^0-related defects energy levels of $MAPbI_3$. The Pb^0 aggregates have a detrimental impact on efficient transport and transfer of electrons and photogenerated carriers at the metal/$MAPbI_3$ interfaces, as they act as interface trap sites and nonradiative recombination sites. This research suggests that the electrical properties of metal/$MAPbI_3$ interfaces are dominated by Pb^0-related defects in $MAPbI_3$, resulting from the interfacial reaction. It also indicates that control of chemical bonding states, especially metal–iodine reactivity, is a key engineering parameter for designing higher performance halide perovskite-based devices.

Experimental section

Synthesis and sample preparation

$CH_3NH_3PbI_3$ ($MAPbI_3$) films were fabricated on p-type Si substrates using one-step spin coating method in a N_2-filled glove box. The $MAPbI_3$ precursor solution was prepared by MAI ($\geq$99%, Sigma-Aldrich) and PbI_2 (99.999% metal basis, Sigma-Aldrich) in molar ratio of 1 : 1 in anhydrous *N*,*N*-dimethlyformamide (DMF) for overall concentration of 40 wt%. The mixed precursor solution was stirred for 24 h under 70 °C on a hot plate in a glove box. Before spin-coating of the $MAPbI_3$ precursor solution, ultraviolet (UV)-O_3 surface treatment was conducted on p-type Si substrates to make the surface of substrates hydrophilic to obtain a uniform and large-grain $MAPbI_3$ film. The $MAPbI_3$ precursor solution was spun onto the p-type Si substrate at a rate of 4000 rpm for 30 s. The films were annealed on a hot plate at 110 °C for 30 min. For metal deposition, the $MAPbI_3$ films were loaded into an ultra-high vacuum thermal evaporation system, which are integrated with the glove box, and Ag, Al, Au, Cr and Ti were deposited on the $MAPbI_3$ films with an equal deposition rate of 0.1 Å s^{-1}. The base pressure of the thermal evaporator was maintained at 10^{-10} mbar and the pressure during metal deposition was less than 5×10^{-7} mbar. The thickness of evaporated metal films was monitored by a quartz crystal microbalance and was also confirmed by X-ray reflectivity measurements.

Metal/$MAPbI_3$ interface characterization

The morphology and crystal structure of $MAPbI_3$ thin films were characterized by scanning electron microscope (SU-70, Hitachi) and X-ray diffraction (D-8 Advance, Bruker Miller). The absorption spectra of MAPbI3 thin films on glass substrates were measured by an ultraviolet-visible photospectrometer (V-740, JASCO). To avoid air and moisture exposure and contamination, the prepared metal (Ag, Al, Au, Cr and Ti)/$MAPbI_3$ thin film samples in glove box were transferred into ultrahigh vacuum chamber for UPS and XPS measurement system *via* a ultra-high vacuum tube ($<10^{-8}$ mbar). The XPS, and UPS analyses were conducted using advanced *in situ* nanosurface analysis system (AISAS, KBSI, Korea). XPS was performed using an AXIS Ultra DLD model (KRATOS, U.K.) operating at a base pressure of 5×10^{-10} mbar at 300 K with a monochromatic Al Kα line at 1486.69 eV. UPS was performed using a He I (21.2 eV) source. The results were corrected for charging effects using Au 4f as an internal reference. The binding energies of all UPS and XPS spectra were calibrated and referenced to the Fermi level (E_F) of the analyzer. A time-of-flight secondary ion mass spectroscopy (IONTOF, Germany) used for chemical depth profile of Ti/$MAPbI_3$, Ag/$MAPbI_3$, and Au/$MAPbI_3$ interfaces with Cs^+ primary ions (1 keV, 100 nA, 500 × 500 μm^2) for the erosion and a Bi^+ pulsed primary ion beam (30 keV, 1 pA, 100 × 100 μm^2) for the analysis. Measurements were collected

in non-interlaced mode to minimize beam damage from the primary beam.

Conflicts of interest

The authors declare no competing financial interests.

Acknowledgements

This work was financially supported by the Future Material Discovery (2016M3D1A1027666) Program, the Basic Research Laboratory (2018R1A4A1022647), and the National Research Foundation of Korea (NRF) grant funded by the Korean government MSIT (2019M3E6A1103818). K. S. C. acknowledges financial support from the Basic Science Research Program through the National Research Foundation of Korea funded by the Ministry of Science and ICT (NRF-2017M3A7B4049176). K. H. acknowledges Overseas Postdoctoral Fellowship of Basic Science Research Program through the National Research Foundation of Korea (NRF) funded by the Ministry of Education (2021R1A6A3A03039891). This material is based upon work performed by the Joint Center for Artificial Photosynthesis, a DOE Energy Innovation Hub, supported through the Office of Science of the U.S. Department of Energy under Award No. DE-SC0004993 (K. H. and C. M. S.-F.).

References

1 A. Kojima, K. Teshima, Y. Shirai and T. Miyasaka, *J. Am. Chem. Soc.*, 2009, **131**, 6050–6051.
2 H.-S. Kim, C.-R. Lee, J.-H. Im, K.-B. Lee, T. Moehl, A. Marchioro, S.-J. Moon, R. Humphry-Baker, J.-H. Yum, J. E. Moser, M. Grätzel and N.-G. Park, *Sci. Rep.*, 2012, **2**, 591.
3 M. M. Lee, J. Teuscher, T. Miyasaka, T. N. Murakami and H. J. Snaith, *Science*, 2012, **338**, 643–647.
4 N. J. Jeon, J. H. Noh, Y. C. Kim, W. S. Yang, S. Ryu and S. I. Seok, *Nat. Mater.*, 2014, **13**, 897–903.
5 D. P. McMeekin, G. Sadoughi, W. Rehman, G. E. Eperon, M. Saliba, M. T. Hörantner, A. Haghighirad, N. Sakai, L. Korte, B. Rech, M. B. Johnston, L. M. Herz and H. J. Snaith, *Science*, 2016, **351**, 151–155.
6 H. Min, M. Kim, S.-U. Lee, H. Kim, G. Kim, K. Choi, J. H. Lee and S. I. Seok, *Science*, 2019, **366**, 749–753.
7 NREL, N., Best Research-Cell Efficiency Chart, US Department of Energy, 2019.
8 W.-J. Yin, T. Shi and Y. Yan, *Adv. Mater.*, 2014, **26**, 4653–4658.
9 S. De Wolf, J. Holovsky, S.-J. Moon, P. Löper, B. Niesen, M. Ledinsky, F.-J. Haug, J.-H. Yum and C. Ballif, *J. Phys. Chem. Lett.*, 2014, **5**, 1035–1039.
10 S. D. Stranks, G. E. Eperon, G. Grancini, C. Menelaou, M. J. P. Alcocer, T. Leijtens, L. M. Herz, A. Petrozza and H. J. Snaith, *Science*, 2013, **342**, 341–344.
11 C. M. Sutter-Fella, Y. Li, M. Amani, J. W. Ager, F. M. Toma, E. Yablonovitch, I. D. Sharp and A. Javey, *Nano Lett.*, 2016, **16**, 800–806.
12 M. A. Green, Y. Jiang, A. M. Soufiani and A. Ho-Baillie, *J. Phys. Chem. Lett.*, 2015, **6**, 4774–4785.
13 J. Choi, J. S. Han, K. Hong, S. Y. Kim and H. W. Jang, *Adv. Mater.*, 2018, **30**, 1704002.
14 J. H. Noh, S. H. Im, J. H. Heo, T. N. Mandal and S. I. Seok, *Nano Lett.*, 2013, **13**, 1764–1769.
15 D. M. Jang, K. Park, D. H. Kim, J. Park, F. Shojaei, H. S. Kang, J.-P. Ahn, J. W. Lee and J. K. Song, *Nano Lett.*, 2015, **15**, 5191–5199.
16 A. Younis, C.-H. Lin, X. Guan, S. Shahrokhi, C.-Y. Huang, Y. Wang, T. He, S. Singh, L. Hu, J. R. D. Retamal, J.-H. He and T. Wu, *Adv. Mater.*, 2021, 2005000, DOI: 10.1002/adma.202005000.
17 Y.-H. Kim, H. Cho, J. H. Heo, T.-S. Kim, N. Myoung, C.-L. Lee, S. H. Im and T.-W. Lee, *Adv. Mater.*, 2015, **27**, 1248–1254.
18 J. Xing, X. F. Liu, Q. Zhang, S. T. Ha, Y. W. Yuan, C. Shen, T. C. Sum and Q. Xiong, *Nano Lett.*, 2015, **15**, 4571–4577.
19 K. C. Kwon, K. Hong, Q. V. Le, S. Y. Lee, J. Choi, K.-B. Kim, S. Y. Kim and H. W. Jang, *Adv. Funct. Mater.*, 2016, **26**, 4213–4222.
20 X. Y. Chin, D. Cortecchia, J. Yin, A. Bruno and C. Soci, *Nat. Commun.*, 2015, **6**, 7383.
21 J. Choi, S. Park, J. Lee, K. Hong, D.-H. Kim, C. W. Moon, G. D. Park, J. Suh, J. Hwang, S. Y. Kim, H. S. Jung, N.-G. Park, S. Han, K. T. Nam and H. W. Jang, *Adv. Mater.*, 2016, **28**, 6562–6567.
22 S. G. Kim, Q. V. Le, J. S. Han, H. Kim, M.-J. Choi, S. A. Lee, T. L. Kim, S. B. Kim, S. Y. Kim and H. W. Jang, *Adv. Funct. Mater.*, 2019, **29**, 1906686.
23 P. Schulz, D. Cahen and A. Kahn, *Chem. Rev.*, 2019, **119**, 3349–3417.
24 S. Wang, T. Sakurai, W. Wen and Y. Qi, *Adv. Mater. Interfaces*, 2018, **5**, 1800260.
25 M.-F. Lo, Z.-Q. Guan, T.-W. Ng, C.-Y. Chan and C.-S. Lee, *Adv. Funct. Mater.*, 2015, **25**, 1213–1218.
26 P. Schulz, L. L. Whittaker-Brooks, B. A. MacLeod, D. C. Olson, Y.-L. Loo and A. Kahn, *Adv. Mater. Interfaces*, 2015, **2**, 1400532.
27 P. Schulz, E. Edri, S. Kirmayer, G. Hodes, D. Cahen and A. Kahn, *Energy Environ. Sci.*, 2014, **7**, 1377–1381.
28 Y. Kato, L. K. Ono, M. V. Lee, S. Wang, S. R. Raga and Y. Qi, *Adv. Mater. Interfaces*, 2015, **2**, 1500195.
29 J. Zhao, X. Zheng, Y. Deng, T. Li, Y. Shao, A. Gruverman, J. Shield and J. Huang, *Energy Environ. Sci.*, 2016, **9**, 3650–3656.
30 L. Zhao, R. A. Kerner, Z. Xiao, Y. L. Lin, K. M. Lee, J. Schwartz and B. P. Rand, *ACS Energy Lett.*, 2016, **1**, 595–602.
31 J. Wang, J. Li, Y. Zhou, C. Yu, Y. Hua, Y. Yu, R. Li, X. Lin, R. Chen, H. Wu, H. Xia and H.-L. Wang, *J. Am. Chem. Soc.*, 2021, **143**, 7759–7768.
32 H. Kim, J. S. Han, J. Choi, S. Y. Kim and H. W. Jang, *Small Methods*, 2018, **2**, 1700310.

33 S. M. Sze and K. K. Ng, *Physics of semiconductor devices*, John Wiley & Sons, 2006.
34 Y. Hu, J. Zhou, P.-H. Yeh, Z. Li, T.-Y. Wei and Z. L. Wang, *Adv. Mater.*, 2010, **22**, 3327–3332.
35 W. A. Laban and L. Etgar, *Energy Environ. Sci.*, 2013, **6**, 3249–3253.
36 W. Peng, L. Wang, B. Murali, K.-T. Ho, A. Bera, N. Cho, C.-F. Kang, V. M. Burlakov, J. Pan, L. Sinatra, C. Ma, W. Xu, D. Shi, E. Alarousu, A. Goriely, J.-H. He, O. F. Mohammed, T. Wu and O. M. Bakr, *Adv. Mater.*, 2016, **28**, 3383–3390.
37 C. Gu and J.-S. Lee, *ACS Nano*, 2016, **10**, 5413–5418.
38 X. Liu, C. Wang, L. Lyu, C. Wang, Z. Xiao, C. Bi, J. Huang and Y. Gao, *Phys. Chem. Chem. Phys.*, 2015, **17**, 896–902.
39 C.-H. Lin, T.-Y. Li, B. Cheng, C. Liu, C.-W. Yang, J.-J. Ke, T.-C. Wei, L.-J. Li, A. Fratalocchi and J.-H. He, *Nano Energy*, 2018, **53**, 817–827.
40 J. Wang, S. P. Senanayak, J. Liu, Y. Hu, Y. Shi, Z. Li, C. Zhang, B. Yang, L. Jiang, D. Di, A. V. Ievlev, O. S. Ovchinnikova, T. Ding, H. Deng, L. Tang, Y. Guo, J. Wang, K. Xiao, D. Venkateshvaran, L. Jiang, D. Zhu and H. Sirringhaus, *Adv. Mater.*, 2019, **31**, 1902618.
41 F. Zu, P. Amsalem, M. Ralaiarisoa, T. Schultz, R. Schlesinger and N. Koch, *ACS Appl. Mater. Interfaces*, 2017, **9**, 41546–41552.
42 F.-S. Zu, P. Amsalem, I. Salzmann, R.-B. Wang, M. Ralaiarisoa, S. Kowarik, S. Duhm and N. Koch, *Adv. Opt. Mater.*, 2017, **5**, 1700139.
43 W. M. Haynes, *CRC handbook of chemistry and physics*, CRC press, 2014.
44 X. Li, W. Li, Y. Yang, X. Lai, Q. Su, D. Wu, G. Li, K. Wang, S. Chen, X. W. Sun and A. K. K. Kyaw, *Sol. RRL*, 2019, **3**, 1900029.
45 Q. Wang, Y. Shao, Q. Dong, Z. Xiao, Y. Yuan and J. Huang, *Energy Environ. Sci.*, 2014, **7**, 2359–2365.
46 Q. V. Le, M. Park, W. Sohn, H. W. Jang and S. Y. Kim, *Adv. Electron. Mater.*, 2017, **3**, 1600448.
47 P. Liu, X. Liu, L. Lyu, H. Xie, H. Zhang, D. Niu, H. Huang, C. Bi, Z. Xiao, J. Huang and Y. Gao, *Appl. Phys. Lett.*, 2015, **106**, 193903.
48 H. Ishii, K. Sugiyama, E. Ito and K. Seki, *Adv. Mater.*, 1999, **11**, 605–625.
49 L. Li, X. Liu, L. Lyu, R. Wu, P. Liu, Y. Zhang, Y. Zhao, H. Wang, D. Niu, J. Yang and Y. Gao, *J. Phys. Chem. C*, 2016, **120**, 17863–17871.
50 G. Sadoughi, D. E. Starr, E. Handick, S. D. Stranks, M. Gorgoi, R. G. Wilks, M. Bär and H. J. Snaith, *ACS Appl. Mater. Interfaces*, 2015, **7**, 13440–13444.
51 C. Wagner, W. Riggs, L. Davis, J. Moulder and G. Muilenberg, *Handbook of X-ray Photoelectron Spectroscopy*, PerkinElmer Corp. Eden Prairie, MN, 1979, 38.
52 Z. Huo, C.-k. Tsung, W. Huang, X. Zhang and P. Yang, *Nano Lett.*, 2008, **8**, 2041–2044.
53 J. S. Han, Q. V. Le, J. Choi, H. Kim, S. G. Kim, K. Hong, C. W. Moon, T. L. Kim, S. Y. Kim and H. W. Jang, *ACS Appl. Mater. Interfaces*, 2019, **11**, 8155–8163.
54 R. K. Gunasekaran, D. Chinnadurai, A. R. Selvaraj, R. Rajendiran, K. Senthil and K. Prabakar, *Chem. Phys. Chem.*, 2018, **19**, 1507–1513.
55 L. J. Brillson, *Phys. Rev. Lett.*, 1978, **40**, 260.
56 F. Chen, R. Schafranek, W. Wu and A. Klein, *J. Phys. D: Appl. Phys.*, 2011, **44**, 255301.
57 J. F. McGilp, *J. Phys. C: Solid State Phys.*, 1984, **17**, 2249.
58 W. Ming, D. Yang, T. Li, L. Zhang and M.-H. Du, *Adv. Sci.*, 2018, **5**, 1700662.
59 J. T. Tisdale, E. Muckley, M. Ahmadi, T. Smith, C. Seal, E. Lukosi, I. N. Ivanov and B. Hu, *Adv. Mater. Interfaces*, 2018, **5**, 1800476.
60 K. M. Tracy, P. J. Hartlieb, S. Einfeldt, R. F. Davis, E. H. Hurt and R. J. Nemanich, *J. Appl. Phys.*, 2003, **94**, 3939–3948.
61 A. M. Cowley and S. M. Sze, *J. Appl. Phys.*, 1965, **36**, 3212–3220.
62 S. Gupta, P. P. Manik, R. K. Mishra, A. Nainani, M. C. Abraham and S. Lodha, *J. Appl. Phys.*, 2013, **113**, 234505.
63 T. Gallet, D. Grabowski, T. Kirchartz and A. Redinger, *Nanoscale*, 2019, **11**, 16828–16836.
64 A. Buin, P. Pietsch, J. Xu, O. Voznyy, A. H. Ip, R. Comin and E. H. Sargent, *Nano Lett.*, 2014, **14**, 6281–6286.
65 H. H. Yoon, S. Jung, G. Choi, J. Kim, Y. Jeon, Y. S. Kim, H. Y. Jeong, K. Kim, S.-Y. Kwon and K. Park, *Nano Lett.*, 2017, **17**, 44–49.

